RF Filters with Periodic Passbands for Sparse Fourier Transform-Based Spectrum Sensing

Ruochen Lu[®], Student Member, IEEE, Tomás Manzaneque[®], Member, IEEE,
Yansong Yang[®], Student Member, IEEE, Jin Zhou[®], Member, IEEE, Haitham Hassanieh, Member, IEEE,
and Songbin Gong[®], Senior Member, IEEE

Abstract—This paper demonstrates a passive low-insertionloss (IL) RF filter with periodic passbands and capable of sparsifying the spectrum from 238 to 526 MHz for sparse Fourier transform (SFT)-based spectrum sensing. The demonstrated periodic filter employs LiNbO3 lateral overtone bulk acoustic resonators (LOBARs) with high-quality factors (Qs), large electromechanical coupling (k_t^2) , and multiple equally spaced resonances in a ladder topology. To demonstrate the periodic filter, the LOBARs is first modeled to predict k_t^2 of various tones accurately. The fabricated LOBARs show k_t^2 larger than 1.5% and figure of merits $(Q \cdot k_t^2)$ more than 30 for over 10 tones simultaneously, which agree with our modeled response, and are both among the highest demonstrated in overmoded resonators. The multi-band filter centered at 370 MHz has then been obtained with a passband span of 291 MHz, a spectral spacing of 22 MHz, an IL of 2 dB, FBWs around 0.6%, and a sparsification ratio between 7 and 15. An out-of-band rejection around 25 dB has also been achieved for more than 14 bands. The great performance demonstrated by the RF filter with 14 useable periodic passbands will serve to enable future SFT-based spectrum sensing. [2018-0155]

Index Terms—RF filter, sparse Fourier transform, lithium niobate, microelectromechanical systems, piezoelectricity, lateral overtone bulk acoustic resonator.

I. INTRODUCTION

RECENTLY, the increasing demand for wireless applications requires better spectrum access paradigms for efficient utilization of the radio frequency (RF) spectrum. One promising approach is to adopt a multi-frequency agile dynamic spectrum access scheme, where the users sense the spectrum in real time and communicate within the idle channels [1]. The key technology to a shared-spectrum scenario is a real-time wide-band spectrum sensing system [2]–[5]. However, conventional spectrum sensing solutions using high-speed ADCs for sampling the full spectrum (e.g., GHz-wide) are power hungry with power consumption orders-of-magnitude more than that of typical ADCs for a specific

Manuscript received July 9, 2018; revised July 30, 2018; accepted August 3, 2018. Date of publication August 20, 2018; date of current version October 1, 2018. Subject Editor G. Piazza. (Corresponding author: Ruochen Lu.)

The authors are with the Department of Electrical and Computing Engineering, University of Illinois at Urbana–Champaign, Urbana, IL 61801 USA (e-mail: rlu10@illinois.edu; tmanzane@illinois.edu; yyang165@illinois.edu; jinzhou@illinois.edu; haitham@illinois.edu; songbing@illinois.edu).

Color versions of one or more of the figures in this paper are available online at http://ieeexplore.ieee.org.

Digital Object Identifier 10.1109/JMEMS.2018.2864177

band (e.g., Wi-Fi), and thus is unsuitable for battery-power applications (e.g., handsets) [6]. Recently, an alternative low-power approach using moderate-speed ADCs at a sub-Nyquist rate has been reported by leveraging compressive sensing [7]–[11] or the sparse Fourier transform (SFT) [12]. These two methods, however, assume that the spectrum of interest is already sparse, which is almost never the case for the application-crowded sub-GHz spectrum in densely populated areas. To still harness the potential power-saving using SFT while sensing most of the sub-GHz spectrum, one could sparsify the spectrum in a periodic fashion, as shown in Fig. 1, with an array of multiplexing periodic filters that are offset from each other in center frequency. Such a sparsifying multiplexer essentially divides the spectrum of interest into a few subsets that each have the same total bandwidth (BW) but with a much sparser spectral content. Each output of the multiplexer can be then fed to an SFT engine for analyzing the spectral content, and be later aggregated to form a full analysis of the spectrum. Such a massively paralleled frontend would allow constant and simultaneous monitoring of the entire sub-GHz spectrum with little delay. In applications where some latency in spectrum sensing can be tolerated, a tunable periodic filter can be used to replace a multiplexer to sense the spectrum one subset at a time in a sequential fashion, resulting in even smaller power consumption, less complexity, and low component counts.

Regardless of the operation scenarios, it is evident that one of the main challenges for benefiting from the universal employment of SFT in sub-GHz spectrum sensing is to enable the periodic filtering function without swamping the power saving from using SFT. To this end, the most promising approach is to adopt chip-scale passive RF filters with periodic passbands (Fig. 1). Such a filter should attain a sufficient number of passbands with equal frequency spacing and span a wide frequency range to capture all relevant channels. It also should feature a suitable sparsification ratio, γ (frequency spacing over passband bandwidth), to avoid missing any occupancy information while suppressing other subsets of the spectrum that are outside the passbands. Due to the aforementioned requirements, the conventional and some emerging chip-scale RF filter technologies for handsets, namely thin-film bulk acoustic resonators (FBARs) [13], [14], surface acoustic wave resonators (SAWs) [15], [16], and laterally vibrating resonators (LVRs) [17], [18], are not suitable for spectrum

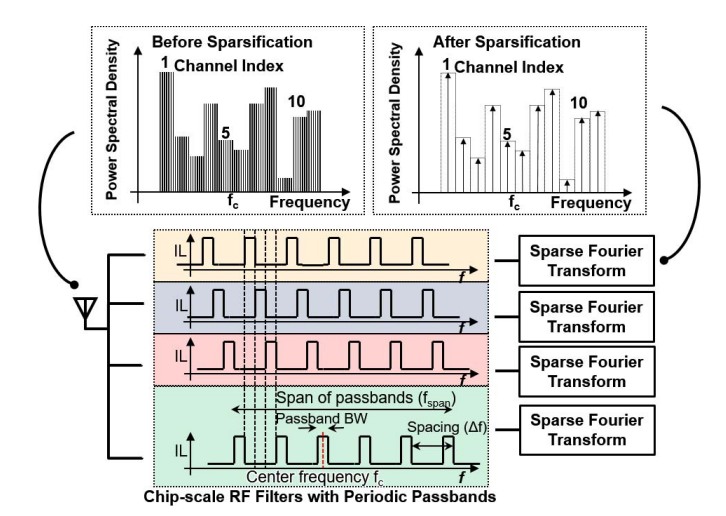


Fig. 1. Block diagram of an energy-efficient spectrum sensing front-end, consisting of a passive RF filter with periodic passband, reconfigurable RF circuits for sparsification. Multiple filters are used to sense the whole spectrum seamlessly. The output signals are used for sparse Fourier transform.

sparsification for two reasons. First, these technologies are optimized to produce a single passband. Thus, enabling multiple periodic passbands would require arraying a series of finetuned filters, resulting in a large form factor and complicated interconnects. Neither scales readily for a wideband spectrum sensing scheme. Second, complex matching networks have to be well designed to minimize the impedance loading effect among parallel-connected single-band filters. It is particularly challenging when the single-band filters are densely packed over a wide frequency range [19], [20].

A more elegant passive filtering solution must be considered for the intended application. To this end, this work aims to leverage the harmonic nature of a resonant cavity to build periodic filters based on the piezoelectric overtone resonators that have an assortment of equally spaced resonances. Overtone or overmoded resonators have been explored in the past for simultaneously attaining multiple resonances with very high Qs. Specifically, high overtone bulk acoustic resonators (HBARs) based on quartz, silica [21], AlN-on-sapphire [22]–[24] and AlN-on-diamond [25], and LiNbO₃ [26], along with lateral overtone bulk acoustic wave resonators (LOBARs) using AlN [27], AlN-on-SiC [28], [29], and AlN-on-sapphire [30], have been demonstrated. However, these devices usually have moderate electromechanical coupling coefficients, k_t^2 , which undermines the capability of these technologies in synthesizing an adequate span of passbands, a sufficiently low IL for each passband, and a reasonable sparsification ratio. The k_t^2 of the previous overmoded resonators is limited because these devices usually combine a piezoelectric thin film of moderate coupling coefficient with a low-damping film in a composite structure to achieve higher Qs but result in a reduced overall k_t^2 for each resonance. This issue can be overcome if a higher- k_t^2 and lower-loss platform is available.

Recently, laterally vibrating devices have been demonstrated on single crystal suspended LiNbO₃ thin films [31]–[35], enabled by advanced thin film transfer techniques [36], [37].

These devices feature very high k_t^2 and low damping simultaneously as evidenced by several recent demonstrations for different modes, including fundamental shear-horizontal mode (SH0) [38]–[45], fundamental symmetric mode (S0) [46]–[48], first-order asymmetric modes (A1) [49]–[51], and thickness-shear mode (TSM) [52]. Overmoding a LiNbO₃ lateral vibrating resonator with large k_t^2 might be the right solution to building overtone resonators and filters for spectrum sparsification. Not surprisingly, a recent report on LiNbO₃ LOBAR has indeed shown simultaneous high k_t^2 (\sim 2%) and Q(>2000) for multiple equally-spaced resonances [53].

This work exploits the LiNbO₃ LOBARs in [53] to demonstrate a passive low-IL RF filter with periodic passbands for SFT-based spectrum sensing. A quantitative analysis of different tones in a LOBAR resonator is first presented to explain the LOBAR design space in the context of synthesizing periodic filters. The filter design is then presented using LOBARs in a ladder topology. In order to validate our design, the standalone LOBARs were fabricated and characterized to show k_t^2 larger than 1.5% and FoMs more than 30 for over 10 tones spanning 330 MHz. The k_t^2 and FoMs are both among the highest demonstrated for overmoded resonators in this frequency range. A periodic filter was subsequently designed, fabricated, and measured to validate the filter level performance based on these high-performance LOBARs. The response of the multi-band filter exhibits 14 passbands from 238 to 526 MHz. They are centered at 370 MHz with a spectral spacing of 22 MHz. Low IL (around 2 dB in dry air, 1.5 dB in vacuum), and FBW around 0.6% (a sparsification ratio between 7 and 15) have been obtained, while an out-ofband rejection around 25 dB has been achieved for more than 14 bands.

This paper is organized as follows. Section II introduces the sparse Fourier transform. Section III provides a general discussion and theoretical analysis of the operation principles of LOBARs, including a model for predicting k_t^2 of different order modes. Section IV introduces the design of the RF filter based on optimized LOBARs in a ladder topology. It also presents filter simulations to show that its performance can achieve intended sparsification. Section V offers details of the fabrication process and images of the fabricated devices. Section VI presents the measurement results and discussions on the implemented filter, including scattering parameters (S-parameters) of the resonators and the filter measured in air and vacuum, and temperature stability of the filter. Finally, Section VII summarizes the findings.

II. SPARSE FOURIER TRANSFORM

The sparse Fourier transform (SFT) is an algorithmic framework that enables recovering the spectrum of frequency sparse signals using only a small subset of their samples and with very low computational overhead [54]–[56]. Hence, SFT can recover wideband spectrum without sampling it at the Nyquist rate – i.e., it can acquire large swaths of the spectrum using a few low-speed ADCs. Further, it can compute the Fourier transform of a sparse signal faster than the FFT, reducing baseband processing. An SFT receiver that can capture GHz

of the sparse spectrum using 3– 4 ADCs sampling at MHz rates was demonstrated in [7] and [57].

SFT is similar to past work that proposes using compressive sensing to acquire signals at a sub-Nyquist rate [8]–[10], [58]. However, approaches based on compressive sensing require random sampling of the signal which cannot be done simply by using standard low-speed ADCs. It needs analog mixing at Nyquist rates [8], [10] and expensive processing to recover the original signal which ends up consuming as much power as an ADC that samples at the Nyquist rate [59]. Unlike compressive sensing, SFT does not need analog mixing or random sampling and can work using commodity radio and standard low-speed ADCs.

The SFT algorithm works in three steps: bucketization, estimation, and collision resolution.

A. Bucketization

SFT starts by mapping the spectrum into buckets. This is done by sub-sampling the signal and then performing a small FFT. Sub-sampling in time causes aliasing in frequency. Since the spectrum is sparsely occupied, most buckets will be either empty or have a single active frequency, and only a few buckets will have a collision of multiple active frequencies. Empty buckets are discarded, and non-empty buckets are passed to the estimation step.

B. Estimation

This step estimates the value and frequency number (i.e., location in the spectrum) of each active frequency. In the absence of a collision, the value of an active frequency is the value of its bucket. To find the frequency number, the algorithm repeats the bucketization on the original signal after shifting it by 1 sample. A shift in time causes a phase change in the frequency domain of $2\pi f \tau/N$, where f is the frequency number, τ is the time shift, and N is the Fourier Transform size. Thus, the phase change can be used to compute the frequency number.

C. Collision Resolution

SFT deals with collisions by performing bucketization multiple times with a co-prime sampling rate with co-prime sizes). The use of co-prime sampling rates guarantees that any two frequencies that collide in one bucketization do not collide in other bucketizations. By iterating between different bucketizations, SFT can recover the entire spectrum.

We described SFT at a very high level. Further details on how to deal with noise, detect collisions, and accurately recover the spectrum can be found in [60]. The above algorithm allows us to sample the signal using low-speed ADCs and recover the spectrum using a logarithmic number of operation making SFT efficient at sampling and computing the frequency representation of the signal. However, SFT requires the input signal to be sparse in the frequency domain which is not necessarily the case in spectrum sensing especially when the spectrum in question is in the sub-GHz region. The RF Filters designed in this paper would sparsify the spectrum

enabling, for the first time, the use of SFT for sensing densely occupied spectrum.

III. LATERAL OVERTONE BULK ACOUSTIC RESONATOR

A. Overview of LOBARs

As discussed earlier, LOBARs have been experimentally studied on different platforms [27], [28], [30]. In this section, we start with a general overview of LOBAR characteristics and qualitative analysis of the critical design parameters. We then present a simplified theoretical model for predicting k_t^2 distribution across different order modes. Based on our model, we design the transducer for our periodic filter application and discuss the possible performance degradation due to deviations in the fabrication process.

As shown in Fig. 2, an SH0 mode LiNbO₃LOBAR consists of a suspended thin film and interdigitated transducers (IDT) that partially cover the top surface. In the context of this work, an IDT is defined as a unit cell between the centers of two adjacent electrodes that are alternatingly connected to the input and ground. The orientation of the device is chosen as -10° to +Y-axis in the X-cut plane of LiNbO₃ for exciting SH0 modes with high k_t^2 [61]. The resonator is mechanically fixed at the two ends in the transverse direction and has mechanically free boundaries in the lateral direction due to the etched edges. The pitch of the transducer is substantially the width of the unit cell, which is also the sum of the electrode width and the gap width between the electrodes. Each IDT introduces electrical fields between its electrodes, which subsequently excite strain and stress standing waves inside the resonator cavity. Single or multiple IDTs can be used in a LOBAR depending on performance requirements. Key parameters of a typical LiNbO₃ LOBAR employing 2 transducers are listed in the inset table of Fig. 2, with the resonator width significantly larger than the transducer pitch and gap width between electrodes.

The admittance response of the LOBAR with its parameters in the inset table of Fig. 2 is simulated with 3-dimensional finite element analysis (FEA) in Coventorware [Fig. 3 (a)]. Compared to a conventional piezoelectric resonator that targets prominent excitation of a single mode, the most remarkable feature of LOBARs is that a number of equally-spaced resonant modes are simultaneously excited. Their stress mode shapes (shear stress T_{xy}) in Fig. 3 (b) indicate that these modes are SHO of different mode orders in the lateral direction. For avoiding ambiguity, these modes are distinguished from each other by their lateral mode orders (m), which are the numbers of displacement nodes/nulls (or stress antinodes) in the lateral direction of their cross-sectional mode shapes.

Such a multi-harmonic nature is universal in a resonant cavity. The various modes are essentially the eigenmodes that can satisfy the boundary conditions of the cavity. In this case, the stress of these modes must vanish at the mechanical free boundaries at the two lateral ends. With a small h/λ (the ratio of film thickness to acoustic wavelength) assumed for the frequency range of interest, the frequencies of various order

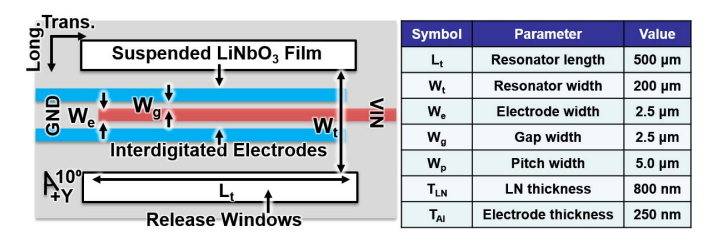


Fig. 2. Schematic of a LiNbO₃ LOBAR with key design parameters. A set of typical values is listed in the inset table.

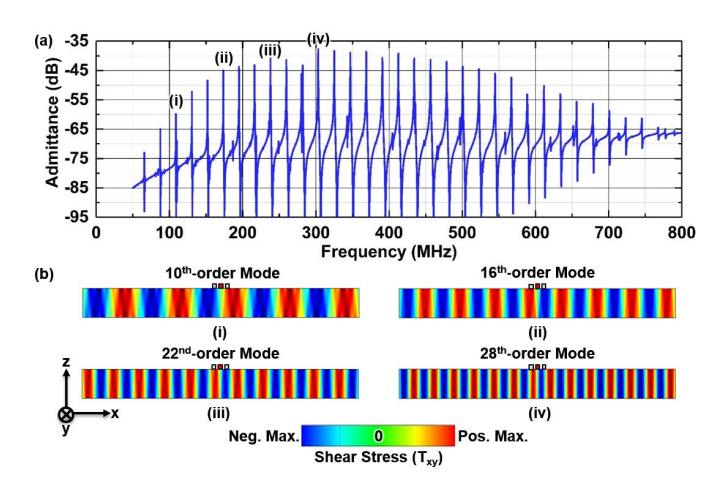


Fig. 3. (a) FEA simulated admittance response of a LOBAR with key parameters listed in the inset table in Fig. 2. (b) Simulated shear stress (T_{xy}) mode shapes for various order SH0 resonances over a wide frequency range.

resonant modes can be approximated by:

$$f_m = \frac{m \cdot v_{\text{SH0}}}{2W_t} \tag{1}$$

where v_{SH0} is the phase velocity of the SH0 mode propagating along the aforementioned orientation of -10° to -Y, m is the mode order, f_m is the resonance of the mth-order mode, and W_t is the width of the resonator body.

Another key observation from Fig. 3 is that only a subset of modes is effectively excited even though additional eigenmodes exist. This limit arises from the fact that a given transducer configuration cannot uniformly couple energy into different order eigenmodes supported by a given resonator cavity. Qualitatively, it is apparent that transducer couples most efficiently to a mode in which the periodicity matches that of the transducer. The resonance of such a mode is considered as the center frequency of the overtone resonator, and is determined by the transducer pitch W_p as:

$$f_c = \frac{v_{\rm SH0}}{2W_p} \tag{2}$$

For the resonance away from the main tone, the mode is less effectively excited, and thus the k_t^2 reduces. One caveat is that the BW of the transducer, which is defined as the frequency range where different modes are excited with no less than half of the k_t^2 of the main tone, will be narrowed if a transducer with large transducer number (N_t) is used. Such dependence of k_t^2 distribution on device configuration and mode order will be quantitatively analyzed in the following two subsections.

To sum up, once a material platform is selected, three key design parameters, namely resonator body width (W_t) , pitch width (W_p) , and transducer number (N_t) determine the resonant frequencies of different order tones, the center frequency of overtone span, and the frequency span of the effectively excited overtones respectively.

B. Modeling k_t^2 Distribution

To design a filter based on the overmoded features of LOBARs, several key parameters of each tone are critical for fine-tuning the performance, namely static capacitance C_0 , quality factor Q, resonant frequency f_m , and electromechanical coupling coefficient k_t^2 . The static capacitance, which determines the port impedance of the filter, is mostly set by the electrode dimensions and device layer stack. Its value has reasonably well modeled based on prior work [62]. The quality factor, affecting the IL of the filter, is collectively determined by various loss mechanisms originated from the materials and design [27]. To accurately predict Q for a given material stack and device design is still challenging and remain active research topic that is not the focus of this work. However, empirically, previous work has been shown Os over 1000 for LOBARs structure [53]. Assuming sufficient k_t^2 can be attained, Qs over 1000 are adequate to produce low IL. As stated in the last subsection, the resonance of each tone can be designed by setting the lateral dimensions.

The remaining obstacle for designing LOBARs for periodic filtering is to capture the k_t^2 distribution among different tones. To avoid time-consuming FEA and understand the k_t^2 distribution, we aim to develop a simplified model with sufficient accuracy by resorting to the Berlincourt formula. It describes the device transduction efficiency in converting electrical energy to mechanical energy via piezoelectricity (k_t^2) by [38]:

$$k_t^2 = \frac{U_m^2}{U_e U_d} = \frac{\left(\int T : d \cdot E dV\right)^2}{\int T : s^E : T dV \cdot \int E \cdot \epsilon^T \cdot E dV}$$
(3)

where U_m is the mutual energy, U_e is the elastic energy, and U_d is the electric energy. T is the stress tensor, and E is the electric field. d, s^E and ϵ^T denote the piezoelectric strain constants, compliance constants at a constant electric field, and permittivity constants at a constant stress respectively. For SH0 modes in our X-cut LiNbO₃ thin film, the electrics fields of interest are predominately in the lateral direction since the film is thin and T_{LN}/W_{ϱ} is small. Meanwhile, the stress field distributions in the transverse and thickness directions follow the same sinusoid function in both the denominator and numerator, which cancels out in Eq. 3. Hence, only the lateral components of E and T fields contribute to the ratio, allowing simplification of the investigation to a 1-D case. In other words, the ratio of volumetric integrations in Eq. 3 can be approximated by ratios of 1-D integrations along the lateral direction (x-axis). Along with the 1-D assumption, two additional assumptions are adopted for simplicity. First, the model assumes decoupled stress and electrical fields, where the electrical fields are approximated to be uniform between electrodes and the stress field follows a sinusoidal curve.

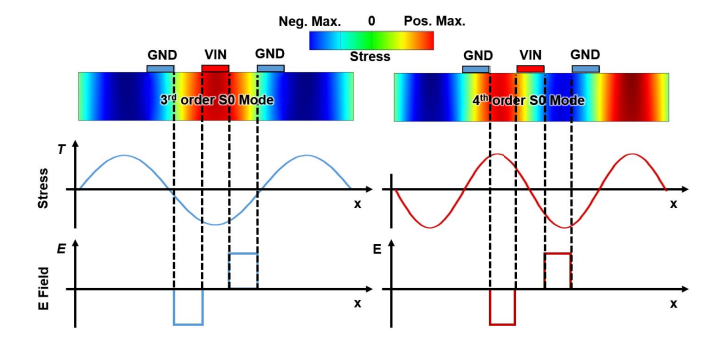


Fig. 4. Simplified stress field and electrical field distribution for both even-order and odd-order modes in a LOBAR with 2 transducers (3 electrodes).

Second, we assume that the phases of the stress are continuous at the interfaces between metalized and free surfaces, which are simplified from the stress continuity and displacement continuity at the interfaces [38]. These two simplifications are typically acceptable for devices with low electromechanical coupling or low electrode coverage [62].

Such a process is showcased in Fig. 4 for a LOBAR device with two transducers and a resonator body width that is five times of the transducer pitch. The decoupled stress and electrical fields are shown for the odd-order mode (e.g., 3rd order) and the even-order mode (e.g., 4th order). The stress fields are sinusoidal with vanishing magnitudes at the mechanically free boundaries, while the electrical fields are uniform between electrodes. The mutual energy is calculated as the integration of the product of these two fields. k_t^2 can be calculated as the mutual energy over the product of the electrical and the mechanical energy. It is also worth noting that the integrated mutual energy for odd-order modes is zero for the 2-transducer configuration, indicating that the oddorder modes cannot be excited with two transducers placed in the center of the device. Following the same rationale, it can be shown that only even-order modes can be excited with even numbers of centered transducers, while only odd-order modes can be excited with odd numbers of transducers. As a result, the frequency spacing (Δf) between adjacent excited modes is:

$$\Delta f = \frac{v_{SH0}}{W_t} \tag{4}$$

The accuracy of the simplified model is first validated via a comparison to FEA results (extracted from simulation shown in Fig. 3). The k_t^2 distribution of different modes is calculated with Eq. 3 and then normalized to the maximum k_t^2 obtained in the FEA simulation. The simplified model shows good agreement with the FEA results. The slight discrepancies are caused by the decoupled assumption used in the model. Note that it is not necessary to use FEA for every simulation with different design parameters after obtaining the constant for normalizing the k_t^2 distribution. Therefore, we have obtained a simplified model with high accuracy for efficiently designing our LOBARs.

It is observed that the resonant mode is most effectively excited when the pitch width matches the acoustic

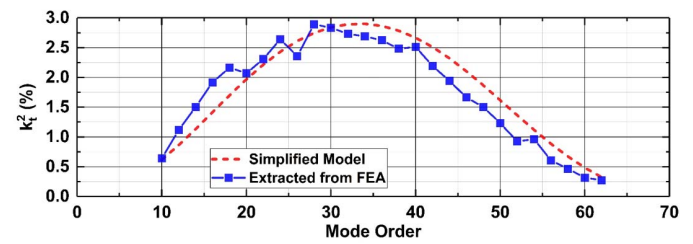


Fig. 5. Comparison of k_t^2 of different even-order modes calculated by different methods, validating the proposed model. The device dimensions are shown in the inset table in Fig. 2.

half wavelength. The coupling decays when the pitch width and the wavelength mismatches, and turns zero when the pitch width is double of the acoustic half wavelength due to the full cancellation of mutual energy. It is also noteworthy that as seen in Eq. 3, the material properties are merely constants in the integration. It implies that the coupling coefficients of the piezoelectric material only determine the absolute amplitude of k_t^2 of each mode, but not the relative distribution over different mode orders. In other words, the distribution is only affected by the LOBAR dimensions, namely resonator body width (W_t) , pitch width (W_p) , and transducer number (N_t) . This assertion is valid as long as the assumption of decoupled stress and electrical fields is acceptable. Detailed discussions on designing N_t will be shown in the next subsection.

C. Transducer Design for Periodic Filters

After obtaining the model for calculating k_t^2 of different order modes in a LOBAR for given dimensions, we design the transducers for LOBARs used in the periodic filter. The key design parameters include the resonator width, the pitch width, and the number of transducers. Targeting a general span from 100 to 800 MHz for periodic passbands with a spectral spacing of 20 MHz between adjacent bands, we set the resonator width to 200 μ m and the pitch width to 5 μ m. To accomplish the design, the transducer number has to be determined. We will compare the merits of different numbers of the transducer in this subsection.

k² distributions of LOBARs with different numbers of transducers are calculated and shown in Fig. 6. To better illustrate the comparison between designs, the figure is normalized to the maximum of k_t^2 attained in the 4-transducer case. The 3-dB BW of k_t^2 of each design is marked in each figure. The absolute BW of each design in the frequency domain is the number of modes in the passband multiply by the frequency spacing between tones (Eq. 4). For the dimension listed in Table I, the 10th to 60th order modes evenly spread from 110 to 660 MHz. It is clear that a larger k_t^2 can be obtained for the tone in the center with more transducers but at the cost of a narrower span over which k_t^2 can be maintained above a certain threshold. It is also noteworthy that the single transducer case features the maximum k_t^2 at the low-frequency end (i.e., lower-order modes). Such results agree with the admittance transfer function for one pair of electrodes in a piezoelectric transducer [40]. For our periodic filter design, we are interested in obtaining adequate sparcification ratio

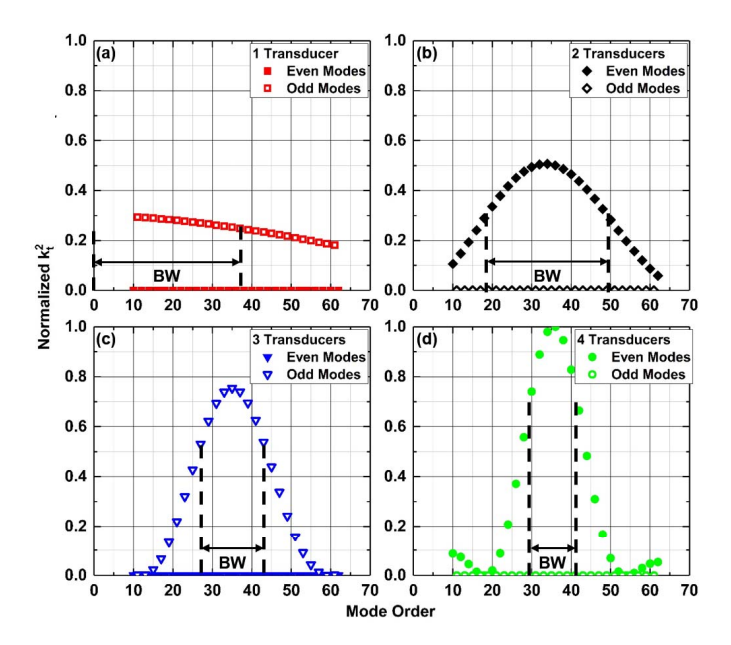


Fig. 6. k_t^2 distribution of different modes in LOBARs with widths that are different numbers of transducers. In each figure, even and odd order modes are marked with solid and hollow symbols, respectively. k_t^2 is normalized to the maximum k_t^2 in the 4-transducer case.

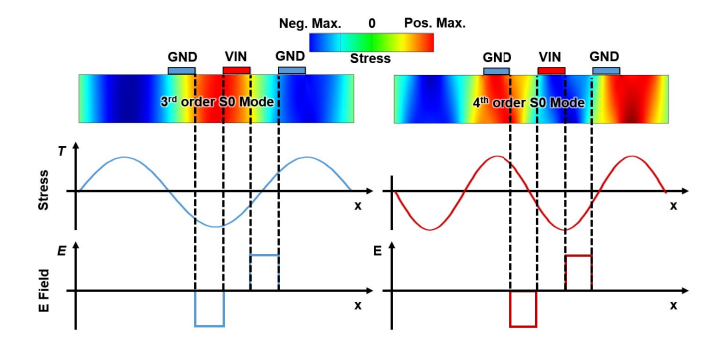


Fig. 7. Simplified stress and electrical field distribution for both even- and odd-order modes in a LOBAR with laterally offset electrode arrangement and 2 transducers. The electrode offset is defined as the lateral shift of the center of the IDTs from the central position of the suspended film.

over a wide range of tones, which is defined as the frequency spacing between adjacent tones (Eq. 4) over the BW of each passband. To achieve sufficient BW for each passband, adequate k_t^2 for each tone is required. Thus, a small transducer number is sought after. However, if we choose a single design, the low-pass behavior seen in Fig. 6(a) rejects signals at a higher frequency, which is not desirable for evenly sampling the signal bands. As a result, 2 transducer design is what we adopt in this work. More details about design considerations for filter's sparcification ratio will be discussed in the next section.

D. Effects of Electrode Offset

The transducer design for our periodic filter has been explored and optimized in this section. However, the previously presented designs are considered in the case where the transducers are centered in the resonator body. By changing the

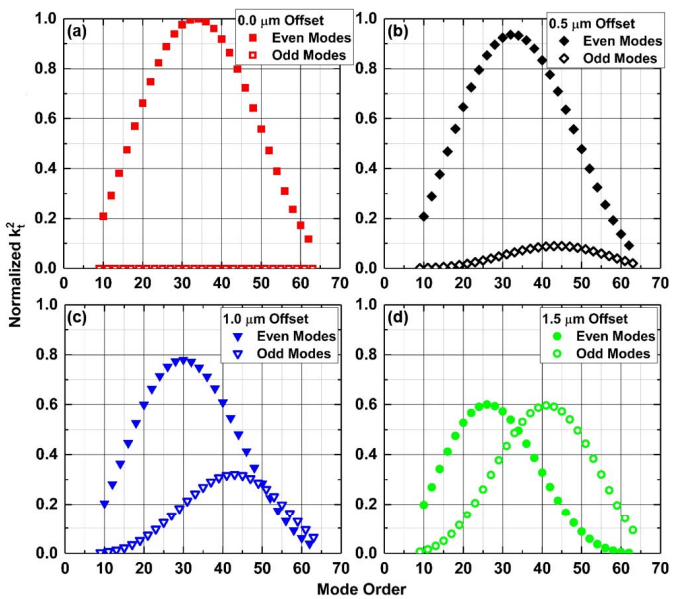


Fig. 8. k_t^2 distribution of different order modes in LOBARs with different lateral electrode offsets. (a) 0 μ m offset. (b) 0.5 μ m offset. (c) 1 μ m offset. (d) 1.5 μ m offset. Even and odd order modes are marked with solid and hollow symbols, respectively, in each figure. k_t^2 is normalized to the maximum k_t^2 in the perfectly-aligned case.

electrode offset of the electrode, another degree of freedom in the design can be unlocked. This effect is shown in Fig. 7 with the same model as in Fig. 4, but with an offset electrode. Such deviations break the symmetry in the stress and electric field distribution in the device. As a result, the integrated term using Eq. 3 leads to non-zero results for both even and odd order tones.

Such effects can also be numerically analyzed with the model presented in this section. For example, the 2 transducer case is simulated at different electrode offset, varying from 0.0 μ m to 1.5 μ m [Fig. 8 (a) – (d)]. Compared to a zero-offset case [Fig. 8 (a)], the maximum k_t^2 keeps degrading with a larger offset. The undesired modes (even order modes for odd transducer cases and odd order modes for even transducer cases) are excited with larger k_t^2 . The phenomenon is more obvious for the higher order modes, whose wavelengths are relatively small compared to the electrode offset.

It might be useful for other applications, such as reconfigurable oscillators, to use offset electrodes to increase the mode density in the spectrum [53]. However, in terms of our particular application of periodic filters, it is undesirable to have electrode offset. The reason is that the adjacent modes (one even and one odd order mode) have dramatically different k_t^2 , which makes the design of the filter passband BW difficult. Besides, the small k_t^2 of the not fully harnessed modes reduces the out-of-band rejections. As a result, precise alignment is key to the experimental validation.

To sum up, we have introduced the concept and design of key parameters in a LOBAR. To investigate the k_t^2 distribution among different modes for better designing filters, a simplified model based on Berlincourt formula is presented. Based on the model and the actual need in the periodic filter,

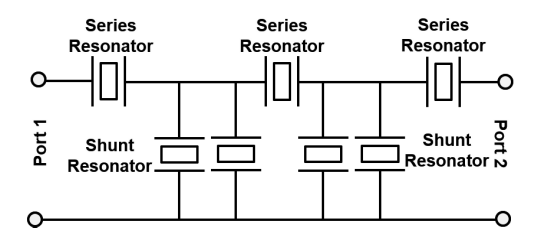


Fig. 9. Ladder filter topology consisting of 3 series resonators and 4 shunt resonators. The shunt resonators are grouped in 2 pairs. The input and output ports of the filter are labelled in the figure.

the transducer and resonator dimensions are set as listed in the table in Fig. 2, with 2 transducers chosen after comparing with other options. Finally, we investigate the effects of the possible deviations in the fabricated devices from the design, which is the transducer offset from the center. It is noteworthy that the method presented in this section is not only a valuable guide for designing LOBARs in filters with periodic passbands. It can also serve as a general guide for other applications using LOBARs or other overmoded devices for high *Q* signal synthesis and reconfigurable communication systems.

IV. RF FILTER WITH PERIODIC PASSBANDS

A. Ladder Filter Design

In the last section, we have discussed the design and simulated performance of LOBARs. In this section, we aim to translate the multi-mode resonator performance to a filter with multiple passbands over a wide frequency range.

Several types of filter topologies have been considered for piezoelectric acoustic resonators, including self-cascaded filters [63], ladder filters [64], and lattice filters [34]. Among them, ladder filters can best harness k_t^2 of one-port resonators for large fractional bandwidth (FBW, defined as the ratio of the 3 dB bandwidth to the passband center frequency) without resorting to complex or differential routing, and achieve high out-of-band rejection at the same time. Thus, they are most suitable for constructing sparsification filters. The circuit schematic of the designed ladder filter is shown in Fig. 9, consisting of 3 series resonators and 4 shunt resonators (grouped in 2 pairs). More shunt resonators are used to create larger out-of-band rejection [47].

To create passbands, the series resonances of the series resonators should be slightly higher than the series resonances of the parallel resonators. For a conventional ladder filter with a single passband, the BW reaches a maximum when the series resonances of the series resonators align with the parallel resonances of the shunt resonators. Considering that k_t^2 sets the separation between series and parallel resonances, the maximum FBW can be approximated by:

$$FBW \approx k_t^2/2 \tag{5}$$

If the frequency offset between series and shunt resonators exceeds the maximum bandwidth allowed by device k_t^2 , a dip will emerge in the center of the passband. On the other hand, if the frequency offset is smaller than the maximum FBW,

the obtained FBW will be set by the resonances of the series and shunt resonators, as:

$$FBW = \frac{2(f_s - f_p)}{f_s + f_p} \tag{6}$$

Thus, accurately setting the resonances of both resonators for multiple modes is essential for designing our ladder filters with periodic passbands. Recalling Eq. 1, such a desired frequency offset can be achieved by either changing the effective phase velocity v_{SH0} or resonator body width W_t . To avoid fabrication complexity and leverage the monolithic frequency diversity of laterally vibrating resonators, we choose to lithographically set the lateral dimensions (W_t) of the series and shunt resonators slightly differently. In order to have roughly the same multi-mode performance with comparable k_t^2 for various order modes, other design parameters of the series and shunt resonators are kept identical. By combining Eq. 1 and Eq. 6, we have the FBW for any given order mode as:

$$FBW = \frac{2\left(1/W_{t_{series}} - 1/W_{t_{shunt}}\right)}{1/W_{t_{shunt}} + 1/W_{t_{series}}} \approx \Delta W_t/W_t \tag{7}$$

where W_{tshunt} and $W_{tseries}$ are the resonator widths of the shunt and series resonators respectively. ΔW_t is the width difference. The approximation is valid when the width difference is small ($\Delta W_t << W_t$).

To determine the FBW and subsequently the ΔW_t , we have to consider the non-uniform k_t^2 over different order modes. It limits our capability in fully leveraging the k_t^2 of each mode and simultaneously achieving the maximum bandwidth allowed for each mode (Fig. 5). Consequently, we can only set the frequency offset and ΔW_t , so as to maximally harness the lowest k_t^2 among the target overtones. Factoring the additional consideration of the parasitic capacitance introduced by the bus lines and impedance matching over wide bandwidth [40], we aim for an FBW of 0.5% for each of the modes from 20th to 48th order. This thus implies a $\Delta W_t/W_t$ of 0.5%, which translates to that the series and shunt resonators are 201 μ m and 200 μ m in width respectively. The sparcification ratio γ from such an approach can thus be approximated by:

$$\gamma = \frac{\Delta f}{FBW \cdot f_m} = \frac{2W_t}{m \cdot \Delta W_t} \tag{8}$$

which indicates that γ is a function dependent on the mode order. It is expected since the higher order passbands, despite having the same FBW, have large BW due to higher center frequencies. Considering the constant Δf and its independence of mode order, γ decreases with respect to the mode order. For a given mode order between 20^{th} and 46^{th} , with $\Delta W_t/W_t$ as 0.5%, γ varies from 20 to 8.6. Understandably, this is not ideal as arraying such periodic filters (as seen in Fig. 1) with frequency offset to either the maximum or minimum γ can be problematic. For instance, using 8 parallel filters, although can seamlessly sparsify the higher portion of the sensed spectrum, would leave deadzones in the lower portion of the sensed spectrum. On the contrary, arraying 20 filters can ensure no deadzones in the lower portion of the sensed spectrum, but would have impedance mismatch at ports over the frequency

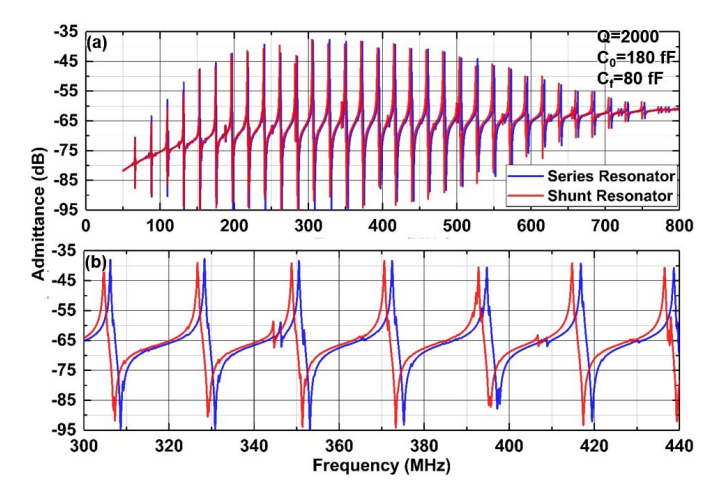


Fig. 10. Simulated admittance responses of the series and shunt resonators used in the ladder filter.

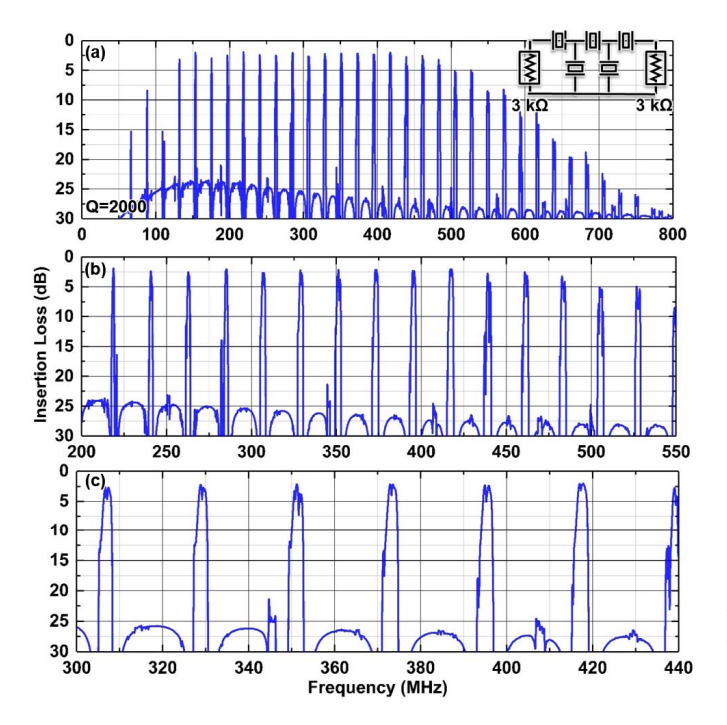


Fig. 11. Simulated IL of the periodic filter. (a) Wide frequency range response. (b) Passbands with low IL. (c) Zoomed-in IL from 300 to 440 MHz.

ranges where the passbands overlap. Unfortunately, this is a limitation of the prototype filter in this work. It might be overcome in the future with a frequency setting scheme that defines the offset proportional to the mode order so that a constant γ can be attained for all passbands. As of now, the prototype shown here could still be proven useful for sensing an allocated spectrum, where missing some spectral segments intended for the guard bands may not affect the detection of occupancy in the allocated bands.

B. Simulated Filter Performance

The simulated resonator responses of the series and shunt resonators are shown in Fig. 10. Qs of different tones are assumed as 2000, and a parasitic capacitance of 80 fF from

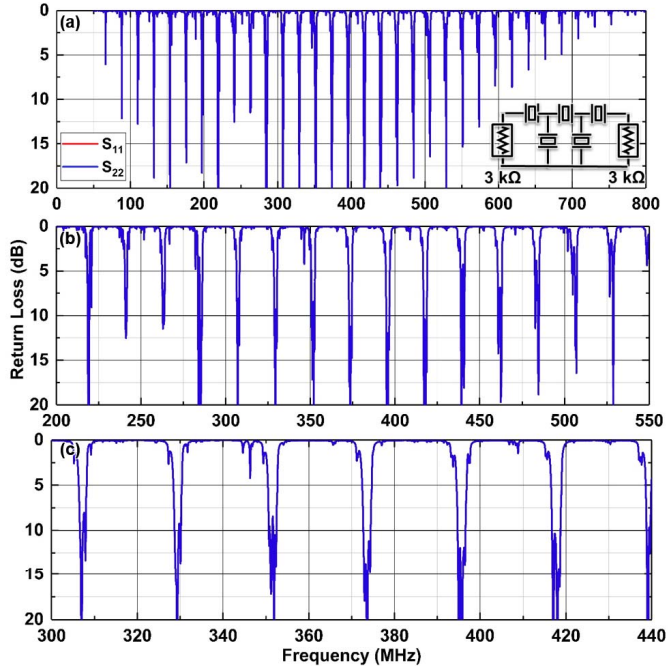


Fig. 12. Simulated return loss of the periodic filter. (a) Wide frequency range response. (b) Passbands with low IL. (c) Zoomed-in IL from 300 to 440 MHz.

the bus lines are included. The simulated results show intended frequency offset between series and shunt resonators.

The filter performance, as shown in Fig. 11 and Fig. 12, is obtained by simulating the ladder filter in the Keysight Advanced Design System with the resonators represented by their FEA simulated S-parameters. A port impedance of 3 k Ω is used on both the input and output to obtain good return loss in each band. The impedance of filter can be reduced to 200-300 Ω over the span of the passband by increasing the size and static capacitance of the resonator or using more parallel resonators [41]. The simulation shows equally spaced passbands with a spectral spacing of 22 MHz. The IL (defined as the minimum loss in the passband) and the FBW of each band are shown in Fig. 13, featuring IL around 2 dB and FBW around 0.5% for more than 15 bands (γ between 8.6 and 20). An out-of-band rejection of about 25 dB is obtained.

V. FABRICATION

The LOBARs and filters were fabricated with a process described in [49]. The fabricated device is composed of an 800 nm LiNbO3 thin film with 250 nm Al electrodes on top. The devices were fabricated using a transferred LiNbO3 thin film on a Si carrier substrate. After etching the release windows using inductively coupled plasma reactive ion etching (ICP-RIE), the top electrodes were sputtered. The devices were finally released by XeF₂ etching.

The optical images and scanning electron microscopy (SEM) images of the fabricated 200- μ m-wide LOBAR are shown in Fig. 14. The parameters are listed in the inset table in Fig. 2. The fabricated filter with periodic passbands is shown in Fig. 15. The shunt and series resonators are arranged in the same row. The input and output ports are marked in the figure.

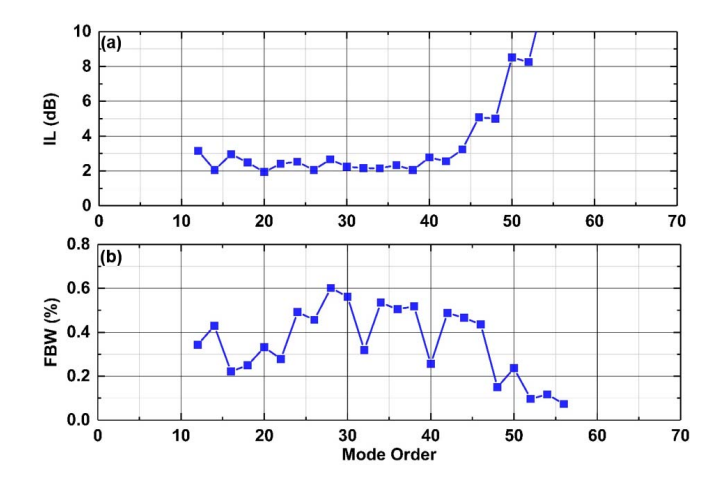


Fig. 13. Simulated IL and 3-dB FBW of various order passbands of the periodic filter. The ripples in the FBW versus mode order are caused by the small IL notches in some of the passbands.

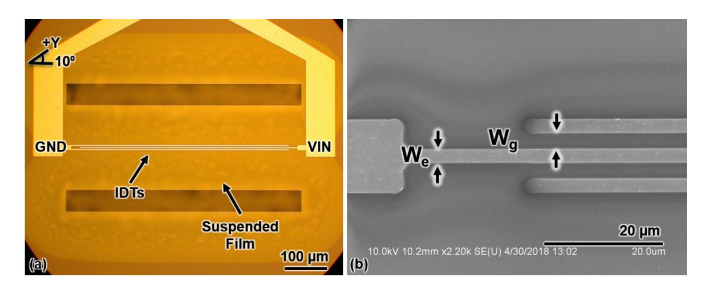


Fig. 14. (a) Optical and (b) SEM images of the fabricated LOBAR.

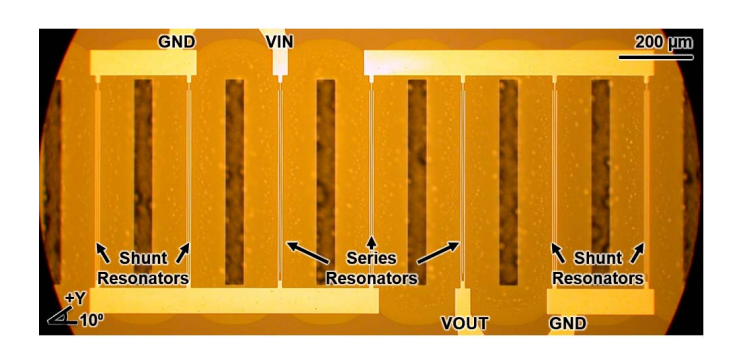


Fig. 15. Optical image of the fabricated LOBAR filter with the design introduced in Section III.

To achieve good alignment in the lateral direction and to eliminate the undesired k_t^2 degradation caused by electrode offset during the fabrication, groups of devices with different electrode offset but the same design were included in the mask. As a result, a device with minimum electrode offset can be expected.

VI. MEASUREMENT AND DISCUSSIONS

A. LOBAR Measurement

The S-parameters of the standalone designed LOBARs (both the series and shunt resonators) were first measured with a Keysight N5249A PNA-X network analyzer and 50 Ω ports in the air. The measurement was performed at -10 dBm input power level. The results are shown in Fig. 16. The

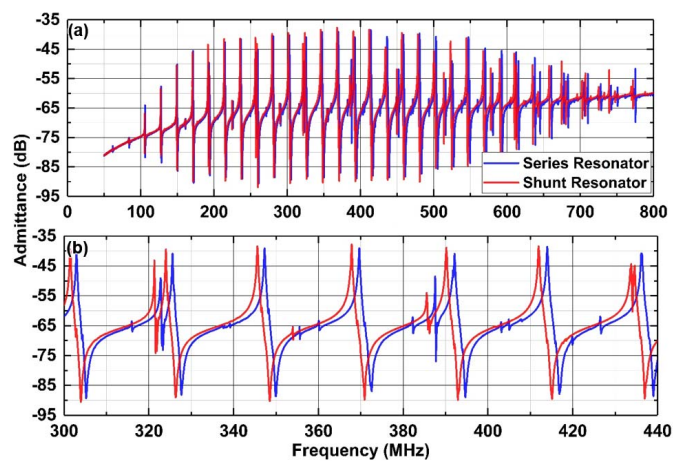


Fig. 16. Measured (a) wide-band and (b) zoomed-in admittance responses of the series and shunt resonators used in the ladder filter.

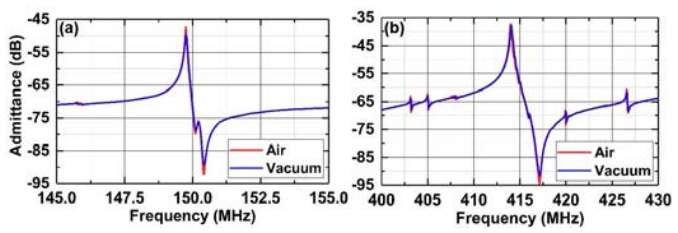


Fig. 17. Zoomed-in admittance responses of the series resonator measured in air and in vacuum. (a) 14^{th} -order mode and (b) 38^{th} -order mode.

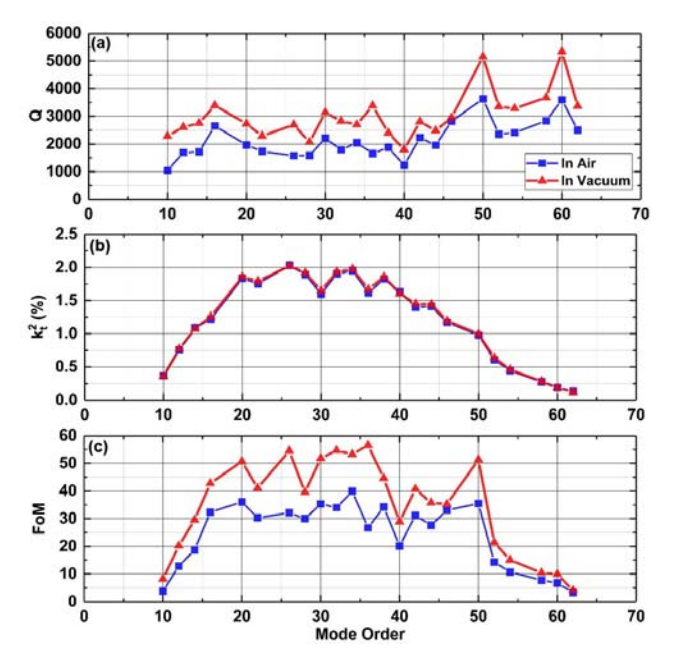


Fig. 18. Q, k_t^2 and FoM of each order extracted from measurements done in dry air and vacuum. The mode order is determined from the resonant frequency of each tone.

measurements show great agreement with results predicted by the FEA simulation. Multiple equally-spaced modes are successfully excited and harnessed by the transducers. The series resonances of the series resonator roughly align with the

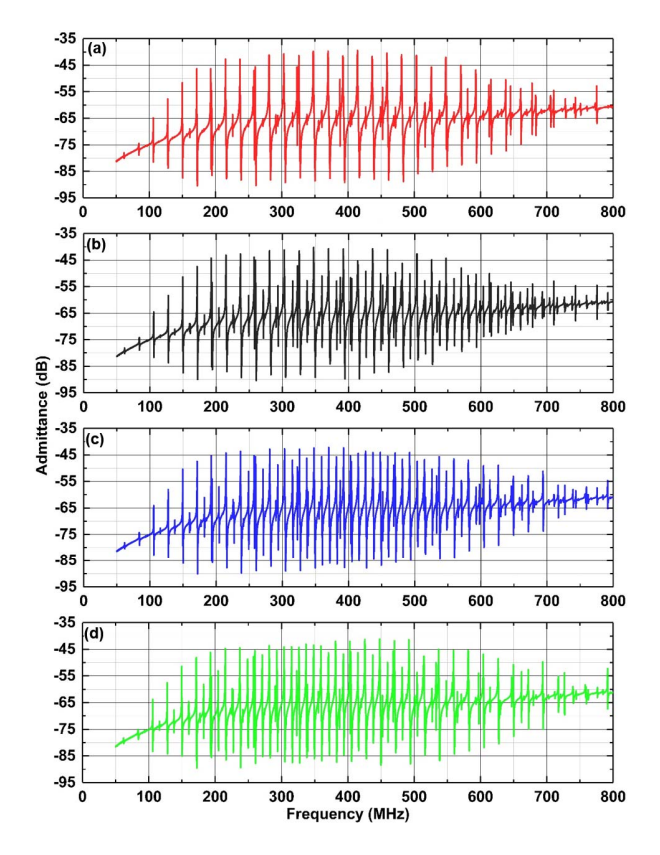


Fig. 19. Measured admittance responses of four different LOBARs with (a) 0 μ m electrode offset, (b) 0.5 μ m electrode offset, (c) 1.0 μ m electrode offset, and (d) 1.5 μ m electrode offset.

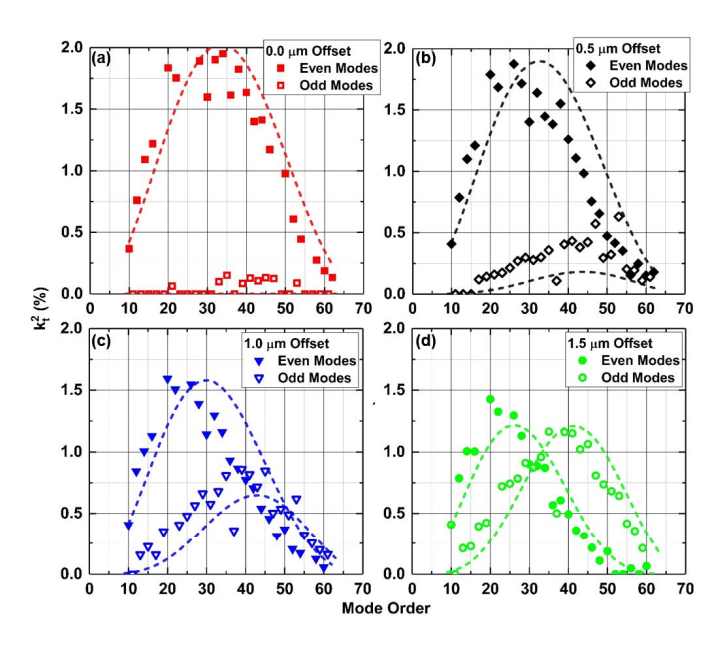


Fig. 20. Measured k_t^2 of different modes in LOBARs with different lateral electrode offsets with even and odd order modes marked with solid and hollow symbols. The calculated k_t^2 distribution is shown in dash lines for both even and odd order modes. The results show good agreement.

parallel resonances of the shunt resonator over the interested frequency range.

Because of the similarities in the performance between the series and the shunt resonators, the series resonator will

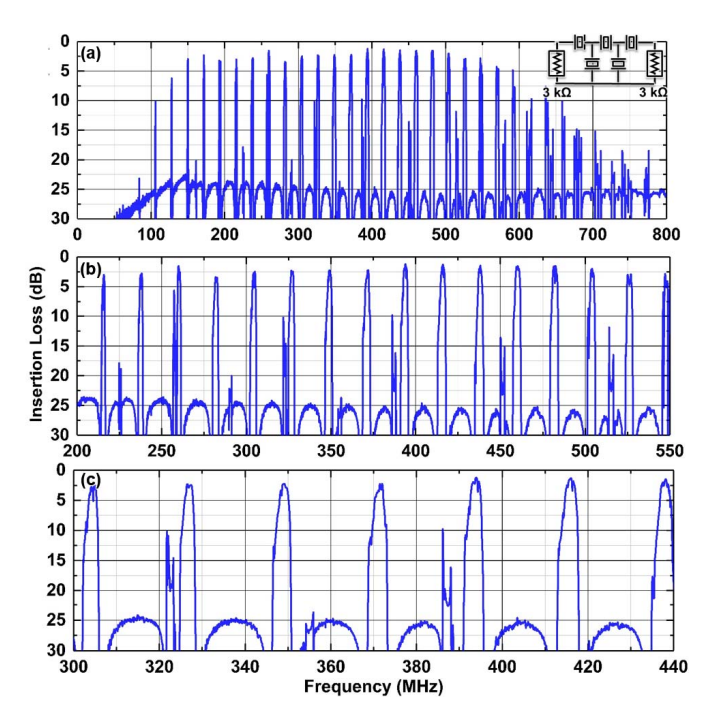


Fig. 21. Measured IL of the filter with periodic passbands. The measurements were done in dry air.

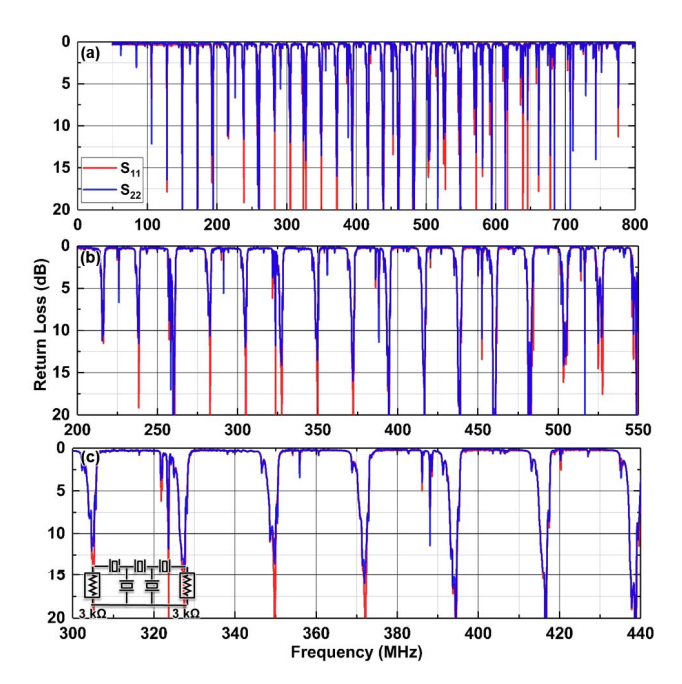


Fig. 22. Measured return loss of the filter with periodic passbands. The measurements were done in dry air.

be introduced with more details in this subsection. The key parameters of each tone were extracted, with 3-dB BW used to calculate Q and the ratio between f_s and f_p for calculating k_t^2 [41]. Such metrology of resonator is valid since the Q is high (>1000) and there are few spurious modes between f_s and f_p . The LOBAR achieved Q_s around 2000 and k_t^2 no smaller than 1% for 16 tones (14th -order mode to 50th-order mode). The measured k_t^2 is 70% of the simulated values due to the existence of parasitic capacitances caused by the

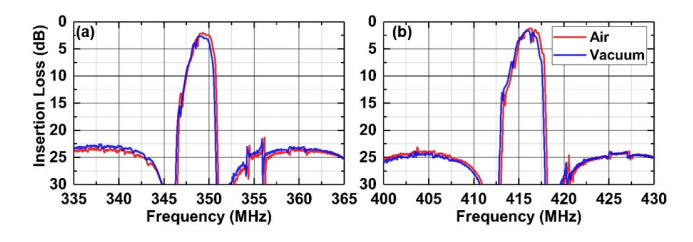


Fig. 23. Zoomed-in IL of the filter measured in air and in vacuum, namely (a) 36th-order mode and (b) 38th-order mode.

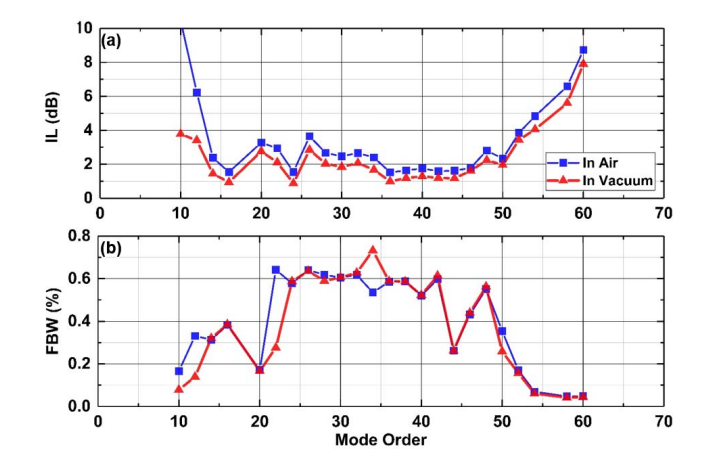


Fig. 24. Measured IL and 3-dB BW of different order passbands in the filter when measured in dry air and measured in vacuum.

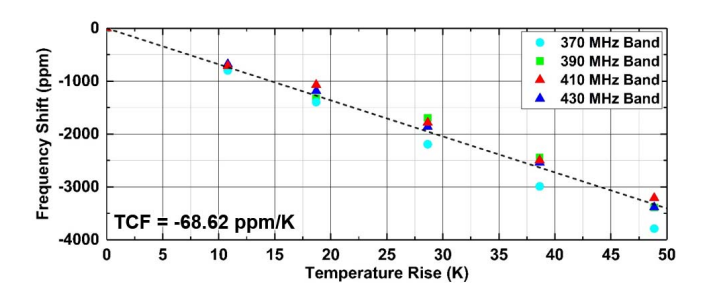


Fig. 25. Measured frequency variation of Device C induced by temperature variation up to 50 K. Linear fitting is applied to the measured points represented by symbols for attaining the TCF.

probing structures. The highest Q of 3633 is obtained for the 50th-order mode, while the highest k_t^2 of 2.02% is obtained for the 26th-order mode. The highest FoM of 39.9 is obtained for the 30th-order mode. A total capacitance (including static and parasitic capacitances) of 260 fF is measured. The Qs are among the highest ever reported in LiNbO₃ resonators, and the FoM are among the highest demonstrated in overmoded resonators.

To explore the loss mechanisms further, additional tests were performed in a Lakeshore TTP-X probe station with controlled pressure. The performance of the series resonator in dry air and under vacuum of $5.4 \cdot 10^{-6}$ mbar is shown in Fig. 17. To better illustrate the difference, a comparison between different parameters of individual tones are shown in Fig. 18. In the vacuum, the highest Q of 5156 is obtained for the 50^{th} -order mode, and the highest FoM of 56.6 is obtained for the 36^{th} -order mode. The Q enhancement indicates air

TABLE I LOBAR RESONATOR PARAMETERS IN AIR

Mode	Series Resonator				Shunt Resonator			
Order	f_s (MHz)	Q	$k_t^2(\%)$	FoM	f_s (MHz)	Q	k_t^2 (%)	FoM
10	105.9	1043	0.37	3.83	105.3	717	0.28	2.01
12	127.8	1692	0.76	12.8	127.1	1201	0.37	4.48
14	149.7	1713	1.09	18.6	149.0	1784	0.48	8.65
16	171.5	2652	1.22	32.3	170.6	1963	1.16	22.8
18	192.8	-	-	-	191.7	-	-	-
20	214.9	1965	1.83	36.0	213.8	1636	1.89	30.9
22	236.8	1729	1.75	30.3	235.6	1184	1.78	21.0
24	259.6	-	-	-	258.3	-	-	-
26	280.7	1582	2.03	32.1	279.2	1147	2.26	25.8
28	303.0	1586	1.89	29.9	301.4	1221	2.01	24.5
30	325.6	2210	1.6	35.3	324.0	2130	1.7	36.2
32	347.3	1788	1.9	34.0	345.6	1459	2.04	29.7
34	369.7	2047	1.95	39.9	367.8	1865	2.01	37.5
36	392.2	1654	1.61	26.7	390.1	1333	1.69	22.5
38	414.0	1876	1.82	34.2	411.9	1457	1.88	27.4
40	436.2	1229	1.64	20.1	433.7	1242	1.79	22.1
42	458.7	2228	1.4	31.2	456.3	1694	1.42	24.0
44	480.6	1955	1.41	27.6	478.1	1572	1.36	21.4
46	503.0	2820	1.17	33.0	500.0	-	-	-
48	524.7	-	-	-	522.8	2123	0.81	17.2
50	547.3	3633	0.98	35.4	544.5	3280	0.55	18.0
52	570.2	2357	0.61	14.3	567.2	1553	0.57	8.7
54	592.7	2410	0.44	10.7	589.8	1761	0.4	7.0
56	612.4	-	-	-	609.6	-	-	-
58	637.9	2833	0.27	7.78	634.8	1719	0.23	3.9
60	660.6	3596	0.19	6.76	657.4	3007	0.14	4.2
62	683.2	2498	0.13	3.33	680.1	-	-	-

damping as one of the main contributors to the loss in the resonator. Other possible enhancements for the device performance include reducing the electrical resistance in the electrodes and better confine the acoustic energy in the resonator body.

B. Electrode Offset Effect

As introduced in Section II, offset electrodes introduce significant differences in the k_t^2 distribution. Therefore, for each resonator design, we set a group of designs with a different preset offset between the electrode layer and the release window layer to ensure good alignment for one device. At the same time, we have obtained a group of the device with different electrode offset for validating our theoretical calculation in Fig. 8. The measured results are shown in Fig. 19, with the transducer offset varying from 0.0 to 1.5 μ m. For a larger electrode offset, more tones (namely the odd order modes) are excited, and the k_t^2 of the even modes decreases. The k_t^2 of different tones is extracted for different offset cases and plotted in Fig. 20 with even and odd modes marked with solid and hollow symbols. The calculated distributions are also plotted with dashed lines in the figures. The results show great agreement between the extracted and calculated values, which further proves our simplified model to be effective in designing LOBARs.

C. Filter With Periodic Passbands Measurement

The filter is first measured with the network analyzer at -10 dBm in dry air. The measurement was performed

TABLE II	
PERIODIC FILTER PARAMETERS IN	Air

Mode Order	f_c (MHz)	IL (dB)	BW (MHz)	FBW (%)
10	105.97	10.47	0.18	0.17
12	127.82	6.23	0.42	0.33
14	149.89	2.38	0.47	0.31
16	171.67	1.55	0.66	0.38
18	192.60	-	1	-
20	215.16	3.27	0.37	0.17
22	238.26	2.94	1.53	0.64
24	260.20	1.55	1.50	0.58
26	282.15	3.65	1.81	0.64
28	304.47	2.67	1.88	0.62
30	326.90	2.48	1.98	0.61
32	349.14	2.66	2.16	0.62
34	371.31	2.40	1.99	0.53
36	393.80	1.53	2.31	0.59
38	415.97	1.64	2.45	0.59
40	438.20	1.76	2.28	0.52
42	460.21	1.59	2.75	0.60
44	482.40	1.62	1.26	0.26
46	503.96	1.79	2.18	0.43
48	526.19	2.81	2.90	0.55
50	547.82	2.33	1.94	0.35
52	569.29	3.85	0.97	0.17
54	591.44	4.83	0.41	0.07
56	610.90	-	-	-
58	636.00	6.59	0.30	0.05
60	658.44	8.73	0.32	0.05
62	681.30	-	-	-

at 50 Ω system, and the port impedance was transformed to 3 k Ω in Advanced Design System for matching both input and output ports. The measured IL and reflections are shown in Figs. 21 and 22. From the results, both ports are well matched. The implemented periodic filter is centered at 370 MHz with a spectral spacing of 22 MHz. Low IL (around 2 dB), and FBWs around 0.6% (sparsification ratio around between 7 and 15) have been obtained, while an out-of-band rejection around 25 dB has been achieved for more than 14 bands. A minimum IL of 1.55 dB is obtained for the 24th-order mode. The highest FBW of 0.64 is obtained for the 22th-order mode.

Similar to the resonator measurement, the performance of the filter was measured in vacuum and compared with the results measured in dry air. Due to less damping in the vacuum, the transmission shows less IL in the passbands (Fig. 23). The parameters of the filter were extracted and plotted against mode order for both the results obtained in the air and in the vacuum (Fig. 24). An IL enhancement over 0.5 dB is observed for most of the tones. A minimum IL of 0.87 dB is obtained for the 24th order mode.

D. Temperature Stability

The temperature stability of our filter was tested in the Lakeshore TTP-X probe station under vacuum with controlled temperature. The measurement starts at room temperature (291 K), and the temperature rises up to 350 K. The frequency point with minimum IL in each band is used to measure the frequency drifting caused by the temperature rise. The measured temperature coefficient of frequency is around

-68.62 ppm/K in 4 bands near the center frequency of the filter (Fig. 25). The value is similar to those reported for SH0 LiNbO₃ resonators and delay lines [34], [40], [65].

VII. CONCLUSION

This work demonstrates a passive low-IL RF filter with periodic passbands for SFT spectrum sensing based on LiNbO₃ LOBARs. To better design, the filter, a quantitative analysis of the k_t^2 distribution of different tones in LOBARs was first developed. Such a model is also helpful for designing overmoded resonators in other applications. The filter with periodic passbands was designed with LOBARs in the ladder topology. Resonators and filters were fabricated to validate our theory. The standalone LOBARs shows high k_t^2 larger than 1.5% and FoM more than 30 for over 10 tones, both among the highest demonstrated in overmoded resonators. The implemented periodic filter is centered at 370 MHz with a spectral spacing of 22 MHz. Low IL (around 2 dB in air, 1.5 dB in vacuum), and FBWs around 0.6% (sparsification ratio between 7 and 15) have been obtained, while an out-ofband rejection around 25 dB has been achieved for more than 14 bands. The great performance will serve to enable future SFT-based spectrum sensing.

REFERENCES

- [1] Second Memorandum Opinion and Order (FCC 10-174), U.S. Government Publishing Office, Washington, DC, USA, 2010.
- [2] J. Mitola and G. Q. Maguire, Jr., "Cognitive radio: Making software radios more personal," *IEEE Pers. Commun.*, vol. 6, no. 4, pp. 13–18, Apr. 1999.
- [3] M. Mishali and Y. C. Eldar, "Wideband spectrum sensing at sub-Nyquist rates [applications corner]," *IEEE Signal Process. Mag.*, vol. 28, no. 4, pp. 102–135, Jul. 2011.
- [4] R. T. Yazicigil, T. Haque, M. R. Whalen, J. Yuan, J. Wright, and P. R. Kinget, "Wideband rapid interferer detector exploiting compressed sampling with a quadrature analog-to-information converter," *IEEE J. Solid-State Circuits*, vol. 50, no. 12, pp. 3047–3064, Dec. 2015.
- [5] A. Pärssinen, "Multimode-multiband transceivers for next generation of wireless communications," in *Proc. Eur. Solid-State Device Res. Conf. (ESSDERC)*, 2011, pp. 42–53.
- [6] 12-Bit, 2.6 GSPS/2.5 GSPS/2.0 GSPS, 1.3 V/2.5 V Analog-to-Digital Converter AD9625 Data Sheet, Analog Devices, Norwood, MA, USA, 2016.
- [7] J. N. Laska, W. F. Bradley, T. W. Rondeau, K. E. Nolan, and B. Vigoda, "Compressive sensing for dynamic spectrum access networks: Techniques and tradeoffs," in *Proc. IEEE Symp. New Frontiers Dyn. Spectr. Access Netw. (DySPAN)*, May 2011, pp. 156–163.
- [8] J. A. Tropp, J. N. Laska, M. F. Duarte, J. K. Romberg, and R. G. Baraniuk, "Beyond Nyquist: Efficient sampling of sparse bandlimited signals," *IEEE Trans. Inf. Theory*, vol. 56, no. 1, pp. 520–544, Jan. 2010.
- [9] J. Yoo, S. Becker, M. Loh, M. Monge, E. Candès, and A. Emami-Neyestanak, "A 100 MHz-2 GHz 12.5x sub-Nyquist rate receiver in 90nm CMOS," in *Proc. IEEE Radio Freq. Integr. Circuits Symp. (RFIC)*, Jun. 2012, pp. 31–34.
- [10] M. Rashidi, K. Haghighi, A. Panahi, and M. Viberg, "A NLLS based sub-Nyquist rate spectrum sensing for wideband cognitive radio," in Proc. IEEE Symp. New Frontiers Dyn. Spectr. Access Netw. (DySPAN), May 2011, pp. 545–551.
- [11] R. T. Yazicigil, T. Haque, M. Kumar, J. Yuan, J. Wright, and P. R. Kinget, "How to make analog-to-information converters work in dynamic spectrum environments with changing sparsity conditions," *IEEE Trans. Circuits Syst. I, Reg. Papers*, vol. 65, no. 6, pp. 1775–1784, Jun. 2018.
- [12] H. Hassanieh, L. Shi, O. Abari, E. Hamed, and D. Katabi, "GHz-wide sensing and decoding using the sparse Fourier transform," in *Proc. IEEE INFOCOM*, Apr./May 2014, pp. 2256–2264.

- [13] R. C. Ruby, P. Bradley, Y. Oshmyansky, A. Chien, and J. D. Larson, "Thin film bulk wave acoustic resonators (FBAR) for wireless applications," in *Proc. IEEE Int. Symp. Ultrason. Symp.*, vol. 1, Oct. 2001, pp. 813–821.
- [14] R. Ruby, P. Bradley, D. Clark, D. Feld, T. Jamneala, and K. Wang, "Acoustic FBAR for filters, duplexers and front end modules," in *IEEE MTT-S Int. Microw. Symp. Dig.*, vol. 2, Jun. 2004, pp. 931–934.
- [15] D. Morgan, Surface Acoustic Wave Filters. Amsterdam, The Netherlands: Elsevier, 2007.
- [16] P. V. Wright, "A review of SAW resonator filter technology," in *Proc. IEEE Ultrason. Symp.*, Oct. 1992, pp. 29–38.
- [17] G. Piazza, P. J. Stephanou, and A. P. Pisano, "Single-chip multiple-frequency AlN MEMS filters based on contour-mode piezoelectric resonators," *J. Microelectromech. Syst.*, vol. 16, no. 2, pp. 319–328, Apr. 2007.
- [18] S. Gong and G. Piazza, "Multi-frequency wideband RF filters using high electromechanical coupling laterally vibrating lithium niobate MEMS resonators," in *Proc. IEEE Int. Conf. Micro Electro Mech. Syst.*, vol. 23, no. 5, Jan. 2013, pp. 785–788.
- [19] P. Warder and A. Link, "Golden age for filter design: Innovative and proven approaches for acoustic filter, duplexer, and multiplexer design," *IEEE Microw. Mag.*, vol. 16, no. 7, pp. 60–72, Aug. 2015.
- [20] G. G. Fattinger et al., "Carrier aggregation and its challenges—or: The golden age for acoustic filters," in *IEEE MTT-S Int. Microw. Symp. Dig.*, May 2016, pp. 1–4.
- [21] H. Zhang, W. Pang, H. Yu, and E. S. Kim, "High-tone bulk acoustic resonators on sapphire, crystal quartz, fused silica, and silicon substrates," *J. Appl. Phys.*, vol. 99, no. 12, p. 124911, 2006.
- [22] W. Pang, H. Zhang, J. J. Kim, H. Yu, and E. S. Kim, "High-tone bulk acoustic resonator integrated with surface micromachined FBAR filter on a single chip," in *IEEE MTT-S Int. Microw. Symp. Dig.*, Jun. 2005, pp. 2057–2060.
- [23] K. M. Lakin, G. R. Kline, and K. T. McCarron, "High-Q microwave acoustic resonators and filters," *IEEE Trans. Microw. Theory Techn.*, vol. 41, no. 12, pp. 2139–2146, Dec. 1993.
- [24] N. Chrétien et al., "Double-port AlN/Sapphire high overtone bulk acoustic resonators for the stabilization of radio-frequency oscillators," in Proc. IEEE Int. Ultrason. Symp. (IUS), Oct. 2012, pp. 2210–2213.
- [25] B. P. Sorokin et al., "AlN/single crystalline diamond piezoelectric structure as a high overtone bulk acoustic resonator," Appl. Phys. Lett., vol. 102, no. 11, p. 113507, 2013.
- [26] M. Pijolat et al., "Large Qxf product for HBAR using Smart Cut transfer of LiNbO3 thin layers onto LiNbO3 substrate," in Proc. IEEE Ultrason. Symp. (IUS), Nov. 2008, pp. 201–204.
- [27] S. Gong, N.-K. Kuo, and G. Piazza, "GHz AlN lateral overmoded bulk acoustic wave resonators with a $f \cdot Q$ of 1.17×10^{13} ," in *Proc. Joint Conf. IEEE Int. Freq. Control Eur. Freq. Time Forum (FCS)*, May 2011, pp. 1–5.
- [28] S. Gong, N.-K. Kuo, and G. Piazza, "GHz high-Q lateral overmoded bulk acoustic-wave resonators using epitaxial SiC thin film," J. Microelectromech. Syst., vol. 21, no. 2, pp. 253–255, 2012.
- [29] M. Ziaei-Moayyed, S. D. Habermehl, D. W. Branch, P. J. Clews, and R. H. Olsson, "Silicon carbide lateral overtone bulk acoustic resonator with ultrahigh quality factor," in *Proc. IEEE 24th Int. Conf. Micro Electro Mech. Syst. (MEMS)*, Jan. 2011, pp. 788–792.
- [30] N.-K. Kuo et al., "Micromachined sapphire GHz lateral overtone bulk acoustic resonators transduced by aluminum nitride," in Proc. IEEE 25th Int. Conf. Micro Electro Mech. Syst. (MEMS), Jan./Feb. 2012, pp. 27–30.
- [31] S. Gong, Y.-H. Song, T. Manzaneque, R. Lu, Y. Yang, and A. Kourani, "Lithium niobate MEMS devices and subsystems for radio frequency signal processing," in *Proc. 60th IEEE Int. Midwest Symp. Circuits Syst.*, Aug. 2017, pp. 45–48.
- [32] R. H. Olsson, III, et al., "A high electromechanical coupling coefficient SH0 Lamb wave lithium niobate micromechanical resonator and a method for fabrication," Sens. Actuators A, Phys., vol. 209, pp. 183–190, Mar. 2014.
- [33] R. Wang, S. A. Bhave, and K. Bhattacharjee, "Design and fabrication of S₀ Lamb-wave thin-film lithium niobate micromechanical resonators," *J. Microelectromech. Syst.*, vol. 24, no. 2, pp. 300–308, 2015.
- [34] S. Gong and G. Piazza, "Design and analysis of lithium-niobate-based high electromechanical coupling RF-MEMS resonators for wide-band filtering," *IEEE Trans. Microw. Theory Techn.*, vol. 61, no. 1, pp. 403–414, Jan. 2013.

- [35] R. Lu, T. Manzaneque, Y. Yang, and S. Gong, "Lithium niobate phononic crystals for tailoring performance of RF laterally vibrating devices," *IEEE Trans. Ultrason., Ferroelectr., Freq. Control*, vol. 65, no. 6, pp. 934–944, Jun. 2018.
- [36] M. Levy et al., "Fabrication of single-crystal lithium niobate films by crystal ion slicing," Appl. Phys. Lett., vol. 73, no. 16, pp. 2293–2295, 1998
- [37] M. Kadota, T. Ogami, K. Yamamoto, H. Tochishita, and Y. Negoro, "High-frequency Lamb wave device composed of MEMS structure using LiNbO₃ thin film and air gap," *IEEE Trans. Ultrason., Ferroelectr., Freq. Control*, vol. 57, no. 11, pp. 2564–2571, Nov. 2010.
- [38] Y.-H. Song, R. Lu, and S. Gong, "Analysis and removal of spurious response in SH0 lithium niobate MEMS resonators," *IEEE Trans. Electron Devices*, vol. 63, no. 5, pp. 2066–2073, May 2016.
- [39] Y.-H. Song and S. Gong, "Wideband spurious-free lithium niobate RF-MEMS filters," J. Microelectromech. Syst., vol. 26, no. 4, pp. 820–828, Aug. 2017.
- [40] T. Manzaneque, R. Lu, Y. Yang, and S. Gong, "Lithium niobate MEMS chirp compressors for near zero power wake-up radios," *J. Microelectro-mech. Syst.*, vol. 26, no. 6, pp. 1204–1215, 2017.
- [41] R. Lu, T. Manzaneque, Y. Yang, and S. Gong, "Exploiting parallelism in resonators for large voltage gain in low power wake up radio front ends," in *Proc. IEEE Int. Conf. Micro Electro Mech. Syst. (MEMS)*, Jan. 2018, pp. 747–750.
- [42] T. Manzaneque, R. Lu, Y. Yang, and S. Gong, "An SH0 lithium niobate correlator for orthogonal frequency coded spread spectrum communications," in *Proc. Joint Conf. Eur. Freq. Time Forum IEEE Int. Freq. Control Symp. (EFTF/IFC)*, Jul. 2017, pp. 143–147.
- [43] R. Lu, T. Manzaneque, Y. Yang, L. Gao, A. Gao, and S. Gong. (Mar. 2018). "A radio frequency non-reciprocal network based on switched acoustic delay lines." [Online]. Available: https://arxiv.org/abs/ 1803.10665
- [44] T. Manzaneque, R. Lu, Y. Yang, and S. Gong, "An SH0 lithium niobate dispersive delay line for chirp compression-enabled low power radios," in *Proc. IEEE 29th Int. Conf. Micro Electro Mech. Syst. (MEMS)*, Jan. 2017, pp. 155–158.
- [45] G. W. Fang, G. Pillai, M.-H. Li, C.-Y. Liu, and S.-S. Li, "A VHF temperature compensated lithium niobate-on-oxide resonator with Q> 3900 for low phase noise oscillators," in *Proc. IEEE Micro Electro Mech. Syst. (MEMS)*, Jan. 2018, pp. 723–726.
- [46] R. Wang, S. A. Bhave, and K. Bhattacharjee, "High k_t²×Q, multi-frequency lithium niobate resonators," in *Proc. IEEE 26th Int. Conf. Micro Electro Mech. Syst.*, Jan. 2013, pp. 165–168.
- [47] S. Gong and G. Piazza, "An 880 MHz ladder filter formed by arrays of laterally vibrating thin film Lithium niobate resonators," in *Proc.* IEEE 27th Int. Conf. Micro Electro Mech. Syst. (MEMS), Jan. 2014, pp. 1241–1244.
- [48] F. V. Pop, A. S. Kochhar, G. Vidal-Alvarez, and G. Piazza, "Laterally vibrating lithium niobate MEMS resonators with 30% electromechanical coupling coefficient," in *Proc. IEEE 30th Int. Conf. Micro Electro Mech. Syst. (MEMS)*, Jan. 2017, pp. 966–969.
- [49] Y. Yang, R. Lu, T. Manzaneque, and S. Gong, "GHz lithium niobate MEMS resonators with FoM of 336 and f.Q of 9.15×10¹²," in *IEEE MTT-S Int. Microw. Symp. Dig.*, Jun. 2018.
- [50] Y. Yang, A. Gao, R. Lu, and S. Gong, "5 GHz lithium niobate MEMS resonators with high FoM of 153," in *Proc. IEEE Int. Conf. Micro Electro Mech. Syst. (MEMS)*, Jan. 2017, pp. 942–945.
- [51] Y. Yang, R. Lu, T. Manzaneque, and S. Gong, "Toward Ka band acoustics: Lithium niobate asymmetrical mode piezoelectric MEMS resonators," in *Proc. IEEE Int. Freq. Control Symp.*, May 2018.
- [52] A. Kochhar, G. Vidal-Álvarez, L. Colombo, and G. Piazza, "Top electrode shaping for harnessing high coupling in thickness shear mode resonators in Y-cut lithium niobate thin films," in *Proc. IEEE Micro Electro Mech. Syst. (MEMS)*, Belfast, Northern Ireland, Jan. 2018, pp. 71–74.
- [53] R. Lu, T. Manzaneque, Y. Yang, A. Kourani, and S. Gong, "Lithium niobate lateral overtone resonators for low power frequency-hopping applications," in *Proc. IEEE 31rd Int. Conf. Micro Electro Mech. Syst. (MEMS)*, Jan. 2018, pp. 751–754.
- [54] H. Hassanieh, P. Indyk, D. Katabi, and E. Price, "Simple and practical algorithm for sparse Fourier transform," in *Proc. 23rd Annu. ACM-SIAM Symp. Discrete Algorithms*, 2012, pp. 1183–1194.
- [55] H. Hassanieh, P. Indyk, D. Katabi, and E. Price, "Nearly optimal sparse Fourier transform," in *Proc. 44th Annu. ACM Symp. Theory Comput.*, 2012, pp. 563–578.

- [56] B. Ghazi, H. Hassanieh, P. Indyk, D. Katabi, E. Price, and L. Shi, "Sample-optimal average-case sparse Fourier transform in two dimensions," in *Proc. 51st Annu. Allerton Conf. Commun.*, Control, Comput. (Allerton), Oct. 2013, pp. 1258–1265.
- [57] O. Abari et al., "A 0.75-million-point Fourier-transform chip for frequency-sparse signals," in *IEEE Int. Solid-State Circuits Conf.* (ISSCC) Dig. Tech. Papers, Feb. 2014, pp. 458–459.
- [58] O. Abari, F. Chen, F. Lim, and V. Stojanovic, "Performance trade-offs and design limitations of analog-to-information converter front-ends," in *Proc. IEEE Int. Conf. Acoust., Speech Signal Process. (ICASSP)*, Mar. 2012, pp. 5309–5312.
- [59] O. Abari, F. Lim, F. Chen, and V. Stojanovic, "Why analog-to-information converters suffer in high-bandwidth sparse signal applications," *IEEE Trans. Circuits Syst. I, Reg. Papers*, vol. 60, no. 9, pp. 2273–2284, Sep. 2013.
- [60] H. Hassanieh, The Sparse Fourier Transform. San Rafael, CA, USA: Morgan & Claypool, 2018.
- [61] I. E. Kuznetsova, B. D. Zaitsev, S. G. Joshi, and I. A. Borodina, "Investigation of acoustic waves in thin plates of lithium niobate and lithium tantalate," *IEEE Trans. Ultrason.*, Ferroelectr., Freq. Control, vol. 48, no. 1, pp. 322–328, Jan. 2001.
- [62] K.-Y. Hashimoto, RF Bulk Acoustic Wave Filters for Communications. Norwood, MA, USA: Artech House, 2009.
- [63] C. Zuo, N. Sinha, and G. Piazza, "Very high frequency channel-select MEMS filters based on self-coupled piezoelectric AlN contour-mode resonators," Sens. Actuators A, Phys., vol. 160, pp. 132–140, May 2010.
- [64] P. Bradley, R. Ruby, J. D. Larson, Y. Oshmyansky, and D. Figueredo, "A film bulk acoustic resonator (FBAR) duplexer for USPCS handset applications," in *IEEE MTT-S Int. Microw. Symp. Dig.*, vol. 1, May 2001, pp. 367–370.
- [65] R. Lu and S. Gong, "Study of thermal nonlinearity in lithium niobate-based MEMS resonators," in *Proc. 18th Int. Solid-State Sens., Actuators Microsyst. Conf. (TRANSDUCERS)*, Jun. 2015, pp. 8–11.



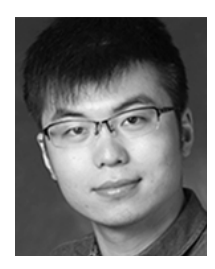
Ruochen Lu (S'14) received the B.E. degree in microelectronics from Tsinghua University, Beijing, China, in 2014, and the M.S. degree in electrical engineering from the University of Illinois at Urbana–Champaign (UIUC), Urbana, IL, USA, in 2017, where he is currently pursuing the Ph.D. degree in electrical engineering. His research interests include radio frequency microsystems and the exploitation of their nonlinearities for timing and signal processing applications. He was a recipient of the 2015 Lam Graduate Award from the College of

Engineering, UIUC, the 2017 Nick Holonyak, Jr. Graduate Research Award, and the 2018 Nick and Katherine Holonyak, Jr. Graduate Research Fellowship from the Department of Electrical and Computer Engineering, UIUC. He has also received the Best Paper Award at the 2017 IEEE International Frequency Control Symposium.



Tomás Manzaneque (M'16) received the Ph.D. degree in industrial engineering from the University of Castilla-La Mancha, Spain, in 2015, with a focus on applying piezoelectric MEMS resonators as sensors for measuring the density and viscosity of liquids. He is currently a Post-Doctoral Researcher with the Micro and Nanotechnology Laboratory, University of Illinois at Urbana–Champaign, USA. He has authored or co-authored over 20 journal papers covering the design, modeling, characterization, and integration of piezoelectric micro-devices.

His main research interest lies in radio frequency acoustic devices for the Internet of Things applications.



Yansong Yang (S'15) received the B.S. degree in electrical and electronic engineering from the Huazhong University of Science and Technology, Wuhan, China, in 2014, and the M.S. degree in electrical engineering from the University of Illinois at Urbana–Champaign, Urbana, IL, USA, in 2017, where he is currently pursuing the Ph.D. degree in electrical engineering. His research interests include design and microfabrication techniques of RF-MEMS resonators, filters, and switches for frontends and wake-up systems. He received the Sec-

ond Place Award in the Best Paper Competition of the 2018 International Microwave Symposium, and was a finalist for the Best Paper Award at the 2018 IEEE International Frequency Control Symposium.



Jin Zhou (S'11–M'17) received the B.S. degree in electronics science and technology from Wuhan University, Wuhan, China, in 2008, the M.S. degree in microelectronics from Fudan University, Shanghai, China, in 2011, and the Ph.D. degree in electrical engineering from Columbia University, New York, NY, USA, in 2017. From 2011 to 2012, he was an RF Integrated Circuits Design Engineer with MediaTek, Singapore. In 2017, he joined the Department of Electrical and Computer Engineering, University of Illinois at Urbana–Champaign, as an Assistant

Professor. He was a recipient of the 2015–2016 Qualcomm Innovation Fellowship and the 2015–2016 IEEE Solid-State Circuits Society Predoctoral Achievement Award. He received the 2015–2016 Jury Award from the Department of Electrical Engineering, Columbia University, for outstanding achievements in the areas of systems, communications, signal processing, and circuits.



Haitham Hassanieh (M'18) received the Ph.D. degree in electrical engineering and computer science from the Massachusetts Institute of Technology (MIT) in 2016. He is currently an Assistant Professor with the Department of Electrical and Computer Engineering, the Department of Computer Science, and the Coordinated Science Laboratory, University of Illinois at Urbana–Champaign. His research focuses on wireless networks, sensing systems, and algorithms. He has received multiple awards, including the 2017 MobiSys Best Paper Award, the 2011

SIGCOMM Best Paper Award, the Sprowls Award for Best Thesis in Computer Science at MIT, the TR10 Award for Technology Review Top 10 Breakthrough Technologies, the NSF Career Award, and the 2016 ACM Doctoral Dissertation Award.



Songbin Gong (S'06–A'09–M'12–SM'17) received the Ph.D. degree in electrical engineering from the University of Virginia, Charlottesville, VA, USA, in 2010. He is currently an Assistant Professor and the Intel Alumni Fellow with the Department of Electrical and Computer Engineering and the Micro and Nanotechnology Laboratory, University of Illinois at Urbana–Champaign, Urbana, IL, USA. His research primarily focuses on the design and implementation of radio frequency microsystems, components, and subsystems for reconfigurable RF

front ends. His research explores hybrid microsystems based on the integration of MEMS devices with photonics or circuits for signal processing and sensing. He was a recipient of the 2014 Defense Advanced Research Projects Agency Young Faculty Award and the 2017 NASA Early Career Faculty Award. Along with his students and post-doctors, he received the Best Paper Award from the 2017 IEEE International Frequency Control Symposium and the second place in the Best Paper Competition from the 2018 IEEE International Microwave Symposium. He has been a Guest Editor of the Special Issue on RF-MEMS in the *Journal of Micromechanics and Microengineering*, and also a Technical Committee Member of MTT-21 RF-MEMS of the IEEE Microwave Theory and Techniques Society, the International Frequency Control Symposium, and the International Electron Devices Meeting.